Journal of Water Process Engineering 56 (2023) 104471

Contents lists available at ScienceDirect

Journal of Water Process Engineering

journal homepage: www.elsevier.com/locate/jwpe

Photoelectrocatalytic based simultaneous removal of multiple organic micro-pollutants by using a visible light driven $BiVO_4$ photoanode

Agha Zeeshan Ali [a,*], Sadhna Jagannathan [b], Yasmina-Doekhi Bennani [b], Jan Peter van der Hoek [a,c], Henri Spanjers [a]

[a] Department of Water Management, Faculty of Civil Engineering and Geosciences, Delft University of Technology, P. O Box 5048, 2600 GA Delft, the Netherlands
[b] Nijhuis Water Technology B.V, Innovatieweg 4, 7007 CD Doetinchem, the Netherlands
[c] Waternet, department of Research & Innovation, P.O. Box 94370, 1090 GJ Amsterdam, the Netherlands

ARTICLE INFO

Keywords:
Organic micro-pollutants
Advanced oxidation process
Photoelectrocatalysis
Dip-coating
$BiVO_4$ photoanode

ABSTRACT

In this research, photoelectrocatalytic (PEC) based advanced oxidation process (AOP) was studied for the removal of multiple OMPs through an oxidative mechanism. This study investigated the application of a $BiVO_4$ photoanode in simultaneous removal of three selected OMPs: acetaminophen (ACT), benzotriazole (BTA) and propranolol (PRO). This study was carried out in demineralized water with a starting concentration of each organic micro-pollutant (OMP) at 45 μg L^{-1}. In order to fabricate $BiVO_4$ photoanodes, a facile and effective dip-coating method was used to deposit $BiVO_4$ photocatalytic layers on fluorine doped tin oxide (FTO) substrate. UV–vis diffusive reflectance spectroscopy, x-ray diffraction (XRD), x-ray photoelectron spectroscopy (XPS) and scanning electron microscopy (SEM) confirmed the successful fabrication of porous $BiVO_4$ photoanode having an absorbance edge at around 526 nm. The fabricated photoanode showed incident photon to current conversion efficiency (IPCE) of 9.23% (λ_{max}=445 nm) under 1 Sun standard illumination. Application of the fabricated photoanodes for the simultaneous removal of ACT, PRO and BTA at an applied voltage of 1 V (vs Ag/AgCl) under solar simulated light resulted in 99% removal of both ACT and PRO, and 70% removal of BTA. The first order rate coefficients and half-life times of ACT and PRO were about three times higher than those of BTA.

1. Introduction

Organic micro-pollutants (OMPs) encompass a range of chemical substances released into water bodies due to human and industrials activities [1]. Depending on the geographic location and the source, the concentration of OMPs found in the surface water or in treated wastewater can vary, however, it is normally between 300 ng L^{-1} and 2 μg L^{-1} [2]. The major categories of OMPs are pharmaceuticals including the endocrine disruptors, skin/body care products and household cleaning products [3]. The toxic effects of consuming OMPs on humans and marine life are still under investigation and for some OMPs such effects have not been studied yet [4]. Different governmental and international environmental regulatory authorities have issued directives that aim to maintain and improve the integrity of water resources and to protect them from OMPs contamination [5]. Industrial and municipal wastewater effluents significantly contribute to the release of OMPs in surface water [2] because the conventional wastewater treatment processes are not completely removing the OMPs [6]. Efforts to remove OMPs from the WWTP effluents or to convert them into less harmful transformation products are increasing to prevent their release to the surface water [7].

Advanced oxidation processes (AOPs) are an effective way to remove OMPs from aqueous solution including municipal or industrial treated wastewater effluents [8]. Photoelectrocatalytic (PEC) based AOP is a type of AOP in which solar irradiation is used to activate photocatalyts to produce reactive species. Semiconducting photocatalytic materials are used as the anode in PEC based AOP to produce in-situ hydroxyl (•OH) and superoxide ($^{\bullet}O_2^-$) radicals which are the main oxidants [9]. The anode in a PEC cell, the photoanode, is in direct contact with the water containing the OMPs and the removal reaction usually occurs at the photoanode-electrolyte interface. The photoanode produces electron-hole pairs upon its interaction with the incoming solar irradiations. Water is oxidized by the photo-generated holes to produce •OH while the dissolved oxygen is reduced by the electrons to generate $^{\bullet}O_2^-$ [10]. According to the literature, •OH play significant role in the unselective oxidation of organic pollutants in aqueous solution [11].

* Corresponding author.
E-mail address: a.aghzeeshan@tudelft.nl (A.Z. Ali).

https://doi.org/10.1016/j.jwpe.2023.104471
Received 17 July 2023; Received in revised form 13 October 2023; Accepted 23 October 2023
Available online 31 October 2023

Organic pollutants are un-selectively oxidized until their complete mineralization or converted into transformation products by the photo-induced oxidants (•OH and $^{\bullet}O_2^-$) [10]. In aqueous solutions, the application of metallic oxide photocatalysts including iron oxide (Fe_2O_3) [12], titanium dioxide (TiO_2) [13], tungsten trioxide (WO_3) [14], zinc oxide (ZnO) [15] and zirconium dioxide (ZrO_2) [16] have been widely studied in literature for the removal of industrial dyes and pharmaceuticals (1–10 mg L^{-1}) by PEC based AOP. These photocatalysts, however, have one major disadvantage that they can only be utilized under the ultraviolet (UV) light (200–400 nm) of the solar spectrum because they have relatively large band gap energy of around 3.0 to 3.5 eV. To overcome the drawback of UV driven photocatalysts, bismuth vanadate ($BiVO_4$), a narrow band gap (approx. 2.4 eV) photocatalyst has emerged as an alternative to UV driven photocatalysts and can be utilized under the visible light of solar spectrum [17]. Apart from $BiVO_4$ applications in water splitting for hydrogen generation, $BiVO_4$ photoanodes are also being utilized for water treatment applications which include the removal of dyes such as methylene blue [18], rhodamine B [19], methyl orange [20] and pharmaceuticals such as tetracycline hydrochloride [21], ciprofloxacin [22] and ibuprofen [23] within a concentration range of 1 to 10 mg L^{-1} from aqueous solution. Removal efficiency of pristine $BiVO_4$ photoanodes is often reduced due to various factors, such as the microstructure of deposited $BiVO_4$ particles and the recombination of photo-generated holes and electrons. These factors contribute to poor charge transport within the photoanode [24]. Several strategies have been explored in the literature to increase the removal efficiencies of $BiVO_4$ photoanodes such as developing a heterojunction of $BiVO_4$ with other suitable photocatalyst [22], doping of $BiVO_4$ [23] and application of a suitable external bias (voltage) [25] to reduce the rate of recombination in the $BiVO_4$ photoanode and ultimately increase the removal efficiency. To the best of our knowledge there is limited research on the application of $BiVO_4$ photoanode for the OMPs removal in the concentration level between 0 and 150 μg L^{-1}. Moreover, there is a lack of literature available on the utilization of $BiVO_4$ photoanodes for the simultaneous removal of multiple OMPs in aqueous solutions.

Benzotriazole (BTA) is an emerging OMP and is frequently detected in surface water resources [26]. Due to its chemical and physical properties it is mostly included as a corrosion inhibiting chemical in e.g. anti-icing fluids and dishwashing detergents [27]. BTA is a polar compound and is highly soluble (1–5 g L^{-1}) in water [29], and it is only partially removed from wastewater during the biological treatment because of its low biodegradability and low adsorption to organic matter [30]. As a result, BTA is released into the environment through WWTP effluents. Within the European Union it is mostly detected at a concentration level of below 50 μg L^{-1} in the aquatic environment [31]. UV/H_2O_2 oxidation [31], catalytic ozonation [32] and photocatalytic based AOP [33] have been applied in few studies on the removal of BTA (1–10 mg L^{-1}) from synthetic and real WWTP effluent. However, there is limited understanding of the removal kinetics of BTA within the concentration range between 0 and 50 μg L^{-1} which is more closer to the concentration level of BTA that could be present in the aquatic environment. Furthermore, there is no literature available on the removal of BTA by PEC based AOP using either UV or visible light driven photoanodes. Propranolol (PRO) is a β-blocker drug that is mainly used for treating hypertension, heart diseases and migraines [34]. Currently PRO is an OMP of concern because of its excessive usage and persistence to conventional wastewater treatment technologies leading to the contamination of WWTP effluent and ultimately surface water with PRO [35]. Polymeric adsorption [36], catalytic H_2O_2 [37], photocatalytic (nano-particles) [38] and electrochemical AOP [39] based removal of PRO (1–20 mg L^{-1}) have been reported in literature. Similarly, acetaminophen (ACT) is also one of the most commonly detected OMPs in surface water, wastewater and drinking water [40]. ACT is mostly purchased without any prescription and is frequently used for pain and fever alleviation [41]. In many European countries WWTPs release a concentration of ACT between 0 and 20 μg L^{-1} in their effluents due to an incomplete removal of ACT [42]. Electrochemical [43] and PEC based AOP [44] have been reported in the literature to remove ACT from real and simulated WWTP effluents. However, there is limited literature on the simultaneous removal of ACT in multiple OMP solutions by PEC based AOP. Investigating the simultaneous removal of multiple OMPs by using a photoanode will give information on the selectivity of the photoanode and the removal kinetics of each OMP present in the aqueous solution. The exposure of all three OMPs (ACT, BTA, PRO) even at lower concentrations of below 200 μg L^{-1} can cause adverse effects on the reproductive system of aquatic organisms [45] and also intake of these OMPs by humans through drinking water can cause inflammation, tissue damage and serious problems in digestion by changing the gut microorganism population [46]. We believe that like other pharmaceuticals, ACT and PRO at a concentration below 150 μg L^{-1} can act additively as a mixture of pharmaceuticals and can cause lethal or sub-lethal toxic effects to aquatic organisms, therefore, their complete removal from surface water should be of significant importance. Moreover, frequent release of these OMPs, even at lower concentrations of below 150 μg L^{-1}, can ultimately result in the accumulation of a mixture of these compounds in surface water resources.

In this research we studied the role of a $BiVO_4$ photoanode in the simultaneous removal of ACT, BTA and PRO each having a starting concentration of 45 μg L^{-1} in demineralized water. ACT, BTA and PRO were selected for this study because of their environmental significance and persistent presence as an OMP in the water resources. Furthermore, BTA and PRO are included in the list of micro-pollutants present in the wastewater provided by the Dutch foundation for Applied Water Research and the Dutch Ministry of Infrastructure and Water Management. First, visible light absorbing photoanodes were fabricated by depositing $BiVO_4$ photocatalytic layer through dip coating method. The structural, morphological, optical and opto-electronic properties of the fabricated photoanodes were analysed and interpreted to validate the successful deposition of $BiVO_4$ photocatalytic layer. Then the photoanodes were employed in a three electrode PEC cell for the simultaneous removal of three OMPs. Energy consumption analysis was also carried out to find the total energy required to remove ACT, BTA and PRO. The removal kinetics of each OMP was assessed by applying a suitable reaction kinetics model. Quenching experiments were performed by using different types of quenching agents to assess the role of oxidants in the removal of selected OMPs by PEC based AOP.

2. Materials and methods

2.1. Materials

All the chemical reagents used in this study were purchased from Sigma Aldrich which include nitric acid (HNO_3) (70%, CAS 7697-37-2), bismuth nitrate pentahydrate ($Bi(NO_3)_3.5H_2O$) (98%, CAS 10035-06-0), vanadyl acetyl acetonate ($VO(acac)_2$) (97%, CAS 3153-26-2), sodium sulfate (Na_2SO_4) (99.0%, CAS 7757-82-6), acetaminophen ($C_8H_9NO_2$) (≥99.0%, CAS 103-90-2), propranolol hydrochloride ($C_{16}H_{21}NO_2$.HCl) (CAS 318-98-9) and benzotriazole ($C_6H_5N_3$) (99%, CAS 95-14-7).

2.2. Preparation of $BiVO_4$ photoanode

A facile dip-coating method was used to deposit a $BiVO_4$ photocatalytic layer on commercially purchased fluorine doped tin oxide (FTO) glass slides (4 × 4 cm; surface resistivity 7 Ω sq.$^{-1}$). Firstly, FTO glass slides were ultrasonically cleaned separately in acetone and ethanol for about 5–6 min. The dip coating solution was prepared by adding 0.049 M bismuth nitrate pentahydrate ($Bi(NO_3)_3.5H_2O$) in 50 mL of ultra-pure water whose pH was adjusted to 2.0–2.2 by using 1 M nitric acid (HNO_3). After adding the $Bi(NO_3)_3.5H_2O$, the solution was thoroughly mixed and then placed in an ultrasonic bath to make it a homogeneous solution. After about 30 min when the solution was clear, 0.049 M vanadyl acetylacetonate was added to the solution, which was

again placed into the ultrasonic bath for homogenous mixing. After about 30 min of utrasonication, the blue coloured solution was taken out, and at this stage the coating solution was ready to deposit $BiVO_4$ on FTO slides. In order to deposit the $BiVO_4$ layer, the FTO glass slide with its FTO side facing upward was dipped into the coating solution for 5 min. After 5 min, the FTO glass slide was removed with the help of a pincer and was placed on a hot plate at 100 °C for 10 min to evaporate the solvent present in the deposited layer. The same procedure of dipping and drying was used to prepare five photoanodes with 1 layer, 2 layers, 3 layers, 4 layers and 5 layers of $BiVO_4$. In the final step, all photoanodes were annealed in an electric furnace at 460°C for 2 h at a ramping rate of 3°C min^{-1}. After the annealing step, the bright yellowish coloured photoanodes were stored in a dry place under normal conditions. Photoanodes with different number of $BiVO_4$ layers were prepared to analyse the effect of layer thickness on the removal efficiency of the photoanodes. $BiVO_4$ photoanode with three layers showed fastest removal of ACT in demineralized water as shown in Fig. S. 1 of supplementary information. Therefore, the three-layer photoanode was selected for further characterization and the application for the removal of selected OMPs by PEC based AOP.

2.3. Structural and morphological characterization

Surface morphology and micro/nano-structure analysis of fabricated photoanodes was carried out by using field emission scanning electron microscopy (SEM), X-ray diffraction (XRD) and X-ray photoelectron spectroscopy (XPS). The detailed description of the characterization techniques is given in our previous research publication [47]. Surface profilometry technique was used to measure the layer thickness of each photoanode by using a Veeco Detak 8 surface profilometer. The results of surface profilometry regarding the layer thickness are shown in Table. S. 1 of the supplementary information.

2.4. Optical and opto-electronic characterization

Optical properties of fabricated photoanodes were studied between 300 and 700 nm (2 nm step size) by using diffusive reflectance UV–vis spectroscopy (LAMBDA 1050+ UV/Vis/NIR spectrophotometer, UV Winlab software). Incident photon-to-electron conversion efficiency (IPCE) was also measured between 280 and 700 nm (10 nm step size) by utilizing a incident photon to current conversion efficiency (IPCE) set-up (specialized for solar cells measurement) under 1 Sun illumination (AM 1.5 standard conditions). IPCE measurement was performed by using the $BiVO_4$ photoanode as working electrode at 1 V (external bias) and a platinum wire as the counter electrode. 0.1 M Na_2SO_4 solution containing 45 μg L^{-1} of ACT was used as electrolyte for IPCE measurements. The IPCE value of the photoanode at each wavelength was calculated by the set-up software using the Eq. (1) and the short circuit current (J_{sc}) was automatically calculated by the software at the end of measurement.

$$\mathrm{IPCE}\% = \frac{\mathrm{I\ (A)}}{\mathrm{P_{in}\ (W)}} \times \frac{1240}{\lambda\ \mathrm{(nm)}} \times 100 \quad (1)$$

I = Photocurrent response at each wavelength.

P_{in} = Input power of the light source at each wavelength.

λ = Wavelength of incoming photons.

Linear sweep voltammetry (LSV) was carried out in a three-electrode cell (dark & light conditions: 60 W m^{-2}) between −0.2 and 1.5 V (vs Ag/AgCl) at a scan rate of 100 mV s^{-1}. Similarly, electrochemical impedance spectroscopy (EIS) under illuminated conditions (60 W m^{-2}) was carried out in a three-electrode cell between 10,000 to 0.01 Hz with a perturbation voltage of 0.2 V, during the measurement the reaction solution was continuously stirred at 600 rpm. For LSV and EIS 0.1 M Na_2SO_4 containing 45 μg L^{-1} of ACT was used as an electrolyte. The data for Mott Schottky plot was obtained under dark conditions by measuring the capacitance of the working electrode ($BiVO_4$ photoanode) within the applied potential range of −1.1 V to 1.1 V vs Ag/AgCl in an electrolyte consisting of a 5 mM solution of $[Fe(CN)_6]^{3-/4-}$ (prepared in 0.1 M KCl) (pH 7.2).

2.5. Photoelectrocatalytic (PEC) experiments

Removal of selected OMPs by PEC based AOP with the use of the prepared photoanodes was carried out by using an Autolab potentiostat (PGSTAT128N) in three electrode cell. The experimental process was similar to our previously published research [47] A quartz reactor cell containing three electrodes and 167 mL of electrolyte solution was used for the PEC based AOP removal experiments. 0.1 M Na_2SO_4 containing ACT, BTA and PRO each with a concentration of 45 μg L^{-1} at a pH of 6.8 was used as electrolyte for the removal experiments. Demineralized water was used for the preparation of the electrolyte. Fabricated photoanodes, Ag/AgCl (3.0 M KCl) electrode and graphite plate (40 × 40 mm) were used as working electrode, reference electrode and counter electrode, respectively. A constant voltage of 1 V vs Ag/AgCl was applied during the removal experiments to minimize the rate of recombination in the fabricated photoanodes. A solar simulator SUNTEST XXL+ having three air cooled 1700 W Xenon lamps emitting 1 Sun illumination spectrum (300–900 nm) was used as light source. The intensity of emitted light between 300 and 400 nm was calibrated to 60 W m^{-2} and the distance between the light source and the photoanode was approximately 15 cm. The reactor cell was placed in a temperature controlled bath at 25 ± 1 °C to perform the removal experiments at constant temperature. Before turning on the simulated solar light and applying the external voltage (1 V), the three-electrode cell containing the reaction solution along with the $BiVO_4$ photoanode, Ag/AgCl reference electrode and graphite cathode was kept under dark conditions for 45 min to analyse the effect of adsorption of OMPs by the components of the reactor cell. After 45 min, the concentrations of the three OMPs were analysed by LC-MS as explained in Section 2.6 and there was no significant change observed in the concentration of the selected OMPs. After 45 min of adsorption time, each removal experiment ran for 2 h with continuous stirring at 600 rpm to increase the mass transfer of OMPs from the bulk to the surface of the photoanode. Samples for the concentration analysis of each OMP were taken at intervals of 30 min. PEC based AOP removal experiments were conducted in triplicate to assess the reproducibility of the results.

Reusability experiments with $BiVO_4$ photoanode were performed by using the same photoanode for four consecutive removal experiments of 2 h each. Between successive experiments the photoanode was rinsed with demineralized water to remove any adsorbed OMP from the photoanode.

2.5.1. Quenching experiments

Quenching experiments were carried out in a similar way as the removal experiments described in Section 2.4, except for the addition of quenching agent in the electrolyte. 4 mM of ethylene diamine tetraacetic acid (EDTA), p-benzoquinone (p-BZQ) and methanol were used in separate experiments to quench photo-generated holes, •OH and $^{\bullet}O_2^-$, respectively. Each experiment ran for 2 h and samples were taken at intervals of 30 min for the concentration analysis of ACT, BTA and PRO.

2.6. Analytical measurement of ACT, BTA and PRO

The concentration of three OMPs in the samples was measured by using liquid chromatography combined with tandem triple-quadrupole mass spectrometry (LC-MS). The complete measurement procedure is described in our previous publication [47]. Based on the measured concentrations of OMPs, removal efficiency of $BiVO_4$ photoanode for each OMP was calculated by using the following equation:

$$\text{Removal efficiency}\ (\%) = \left(1 - \frac{C_t}{C_o}\right) \times 100$$

where C_0 = Initial concentration at time $t = 0$ and C_t = Concentration at any time

3. Results and discussion

3.1. Structure and morphology of photoanodes

Fig. 1 shows the X-ray diffraction peaks of dip-coated $BiVO_4$ photoanode. The main peaks at 18.97°, 28.89°, 30.52°, 34.55°, 35.20°, 39.87°, 42.43°, 46.74°, 47.27°, 51.46° and 59.43° as shown in Fig. 1 were assigned to monoclinic scheelite phase of $BiVO_4$ which was also confirmed by the ICDD database as shown in Fig. S. 2 of the supplementary information. The designated peaks were in agreement with the previous literatures [19,40] and indexed as (110), (121), (040), (200), (002), (211), (015), (240), (042), (161), (321) and (123), respectively. Formation of monoclinic scheelite phase of $BiVO_4$ was desired in this research due to its relatively narrow band gap energy that enables it to have improved interfacial charge transfer properties as compared to tetragonal zircon $BiVO_4$ [48]. The XRD characterization confirmed the successful deposition of $BiVO_4$ without any impurity compound.

Fig. 2 shows the surface morphology of dip-coated $BiVO_4$ photoanode. In low resolution images (Fig. 2 (a) & (b)), the photoanode appeared to have a compact surface with micro sized cracks. These surface cracks increased the roughness and available adsorption surface area of the photoanode for the OMP molecules. The high resolution SEM image in Fig. 2(c) shows the porous layer of $BiVO_4$ particles (under the cracks) that were joined together to form a 3D branch network. The magnified image (Fig. 2 (d)) of the porous layer shows the inter-joining of deposited $BiVO_4$ particles that facilitated efficient charge transport within the photoanode. SEM result exhibited that the porous $BiVO_4$ particles possibly improved the transfer of photo-induced charges from the bulk material to the photoanode-electrolyte interface where they were utilized for the oxidants (•OH and $^{\bullet}O_2^-$) generation. Furthermore, the cracks on the compact layer increased the adsorption surface area available for the BTA, PRO and ACT molecules and this enhanced adsorption of molecules on the surface of the photoanode resulted in a fast and efficient removal of selected OMPs either by direct oxidation through photo-generated holes or by the in-situ produced oxidants. Fig. 2 (2) shows the EDX spectrum of the fabricated photoanode which depicts the elemental analysis of $BiVO_4$ photocatalytic layer, and it is evident from EDX spectrum that only bismuth (Bi), oxygen (O) and vanadium (V) were detected as the major constituent elements in the photoanode. Fluorine doped tin oxide (FTO) was responsible for the detection of Tin (Sn) and calcium (Ca) in the EDX analysis as shown in Fig. 2 (e). The EDX analysis complemented the XRD findings and further corroborated the purity of the $BiVO_4$ deposition without the presence of any impurity element.

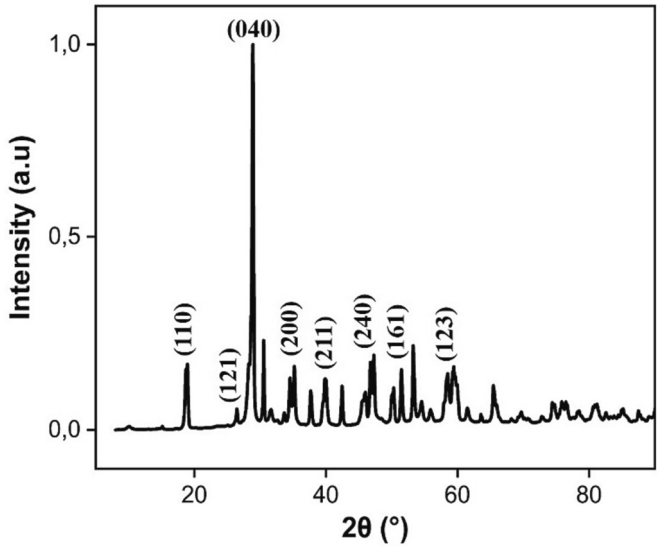

Fig. 1. X-ray diffraction peaksof BiVO4 photocatalytic layer showing the indexed peaks of monoclinic scheelite phase.

The survey scan of X-ray photoelectron spectroscopy (XPS) of the $BiVO_4$ photoanode is shown in Fig. S. 3 of the supplementary information. Fig. S. 3 in supplementary information shows that Bi, O and V were co-existing and exhibited distinct peaks at their respective binding energies. Carbon (C) detected in the XPS survey analysis was considered as an impurity that was present during the analysis. Fig. 3 presents the deconvoluted high-resolution spectra of Bi, V and O. In Fig. 3, the two asymmetric peaks at 162.97 and 157.57 eV represented Bi $4f_{5/2}$ and Bi $4f_{7/2}$ spin orbit splitting states of Bi, respectively. The difference between their binding energies was 5.4 eV, which suggested that Bi was present as Bi^{3+} in the lattice structure of $BiVO_4$ [49]. Similarly, in the case of vanadium (V), the two peaks at 528.42 and 515.22 eV were assigned to V $2p_{1/2}$ and V $2p_{3/2}$ spin orbit splitting states, respectively. Their peak positioning observed in the spectrum suggested that V was present as V^{5+} in the lattice structure of $BiVO_4$ [50]. In the case of oxygen (O) three distinct peaks were observed where each peak represented a different bonding environment around oxygen. The two peaks at 528.05 and 528.85 eV were assigned to oxygen in the lattice structure of $BiVO_4$ and was bonded to Bi and V, respectively. A relatively low intensity peak observed in the O spectrum at 529.95 eV represented the surface adsorbed oxygen [47,51]. Overall, the XPS results successfully confirmed the presence of constituent elements (Bi, O and V) of $BiVO_4$, which was in accordance with the XRD and EDX results.

3.2. Optical and opto-electronic properties of the $BiVO_4$ photoanode

The absorbance spectrum of the $BiVO_4$ photoanode was measured by using UV–vis diffusive reflectance spectroscopy. The absorbance spectrum of the fabricated photoanode is shown in Fig. 4 (a), and it is evident from the spectrum that the photoanode showed strong absorption of incoming photons within the UV–visible range (300–550 nm) of the solar spectrum. The absorbance edge of the $BiVO_4$ photoanode was observed in the visible spectrum of solar irradiation at about 526 nm. The absorbance pattern of the $BiVO_4$ photoanode confirmed that the deposited $BiVO_4$ layer absorbs in the UV–visible range and can be applied for visible light driven PEC based AOP removal of OMPs. The absorbance spectrum in Fig. 4 (a) was also used to determine the approximate band gap energy (E_g) of the fabricated $BiVO_4$ photoanode by using the Eq. (2) as shown below [52]:

$$\alpha h\nu = A\left(h\nu - E_g\right)^{n/2} \tag{2}$$

The Eq. (1) is called as Tauc equation, in this equation: α, h, ν, A and E_g corresponds to absorbance coefficient, Planck's constant, incident light frequency, constant and band gap energy, respectively. The exponent n is a constant and its value depends on the optical transition behaviour of the specific semi-conducting material being used. According to literature, $BiVO_4$ is a direct transition semi-conductor and the value of n for a direct transition semi-conductor is 1 [51]. The E_g was evaluated by substituting the known values in Eq. (2) and a plot of $(\alpha h\nu)^2$ against $h\nu$ was constructed as shown in the inset of Fig. 4 (a). The assessed E_g was found to be 2.36 eV. Result of UV–vis spectroscopy and band gap calculation showed that the dip coating method was successful in fabricating a narrow band gap and a UV–visible light absorbing $BiVO_4$ photoanode.

The calculated band gap energy (E_g) obtained from the inset of Fig. 4 (a) was utilized to determine the valence band (E_{VB}) and conduction band (E_{CB}) edge potentials of the fabricated photoanode. Eq. (3) and Eq. (4) were used to compute E_{CB} and E_{VB} [22]:

$$E_{CB} = X - E_C - 0.5E_g \tag{3}$$

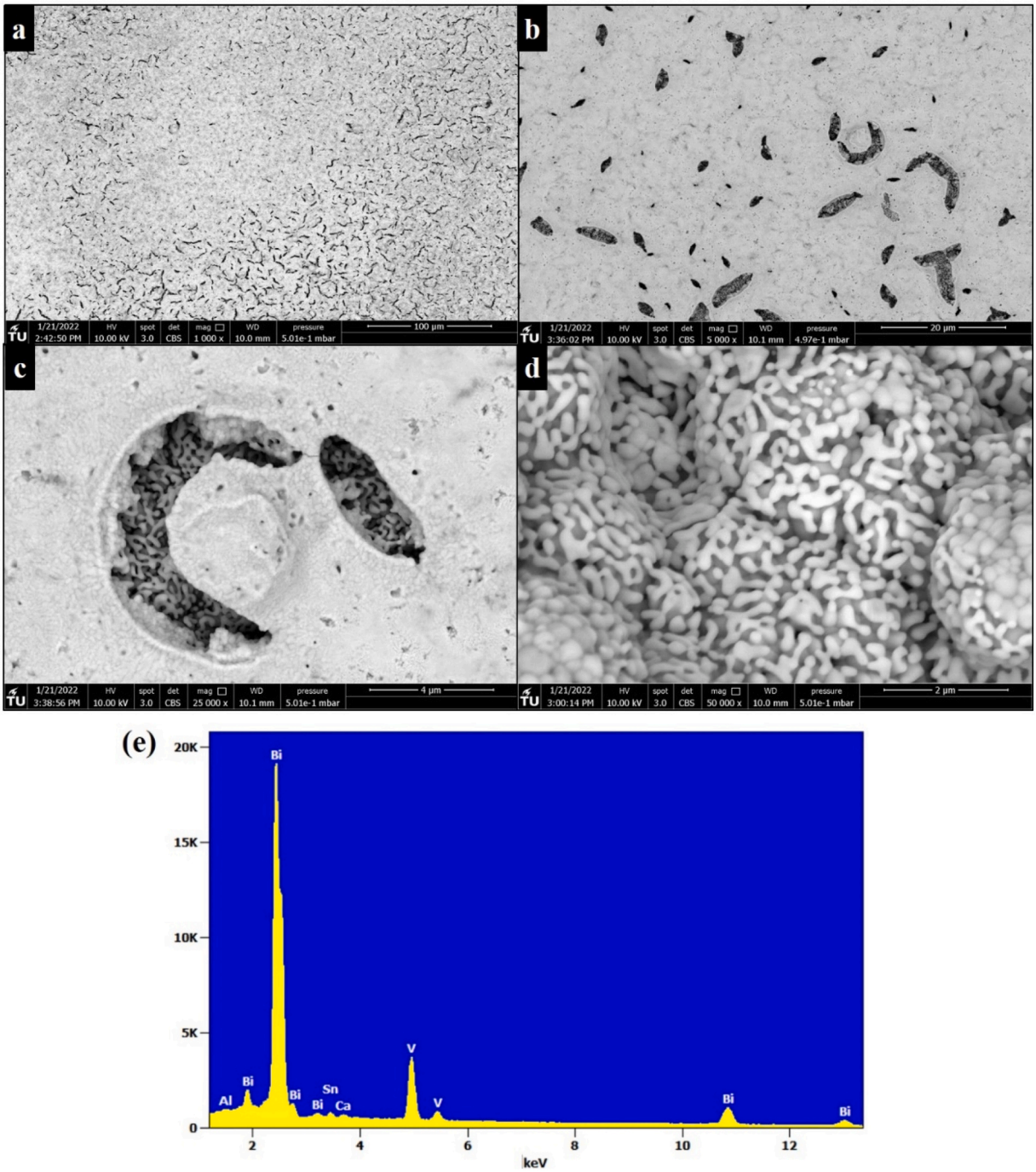

Fig. 2. SEM images showing surface morphology of $BiVO_4$ photoanode at magnification of 1000 x (a) 5000 x (b) 25,000 x (c) 50,000 x (d) and compositional analysis of $BiVO_4$ photoanode through EDX showing the characteristic peaks of constituent elements present in the photocatalytic layer (e).

$$E_{VB} = E_g + E_{CB} \quad (4)$$

In Eq. (3) the variable X represents the geometric mean of the absolute electronegativities of the constituent atoms present in the photocatalyst being used, and for $BiVO_4$ its value is 6.04 eV [53]. In Eq. (3) the E_c corresponds to the energy of free electrons relative to the normal hydrogen electrode and its value is 4.50 eV. E_g in both Eqs. (3) and (4) represents the band gap energy of the $BiVO_4$ photoanode that was obtained from Tauc plot (inset of Fig. 4 (a)). After substituting the known values of E_c, E_g and X in Eqs. (3) and (4), the E_{VB} and E_{CB} for the $BiVO_4$ photoanode were calculated as 2.72 and 0.36 eV, respectively. The calculated band edge potentials were found to be in consistent with the values reported in literature [22] and were able to produce the reactive species to oxidize the OMP molecules as illustrated in Fig. 4 (b).

Linear sweep voltammetry (LSV) technique was used to investigate the influence of the applied voltage on the photo-induced current generated by the $BiVO_4$ photoanode. The LSV plot (Fig. 4 (c)) shows that in dark conditions no photocurrent was generated within the applied potential window of −0.2 to 1.5 V. Fig. 4 (c) shows that in the absence of light, the fabricated photoanode did not act as a classical electro-catalyst for the direct oxidation of OMPs even when an external voltage was applied. In the presence of light (60 W m^{-2}), the applied voltage had a positive impact on the photocurrent of the fabricated photoanode, which confirmed that the applied external voltage decreased the

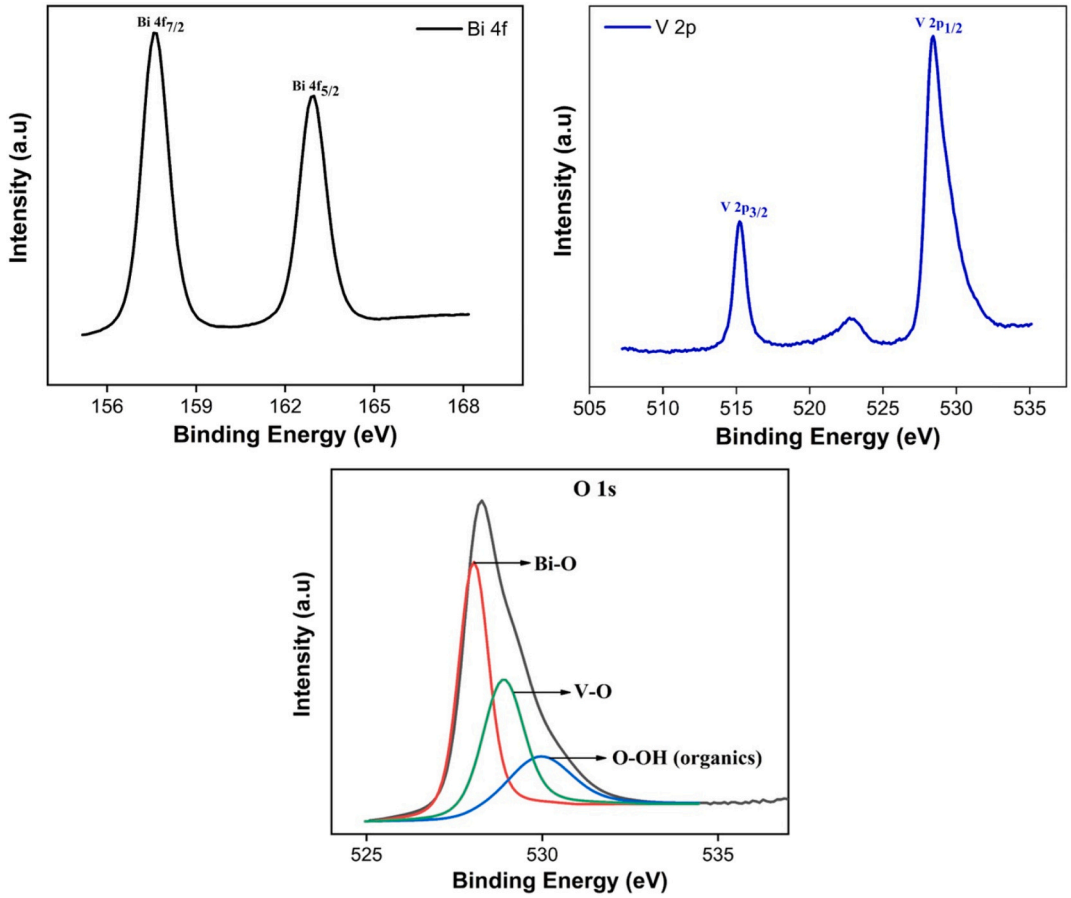

Fig. 3. De-convoluted high resolution XPS spectra revealing Bi $4f_{7/2}$ and Bi $4f_{5/2}$ spin orbit splitting states for Bi, V $2p_{3/2}$ and V $2p_{1/2}$ spin orbit splitting states for V and different chemical bonding environment around O in the lattice structure of $BiVO_4$.

recombination of photo-generated charge carriers in the $BiVO_4$ photoanode. Furthermore, the LSV plot also revealed that photocatalytic removal of OMPs was not possible as no photocurrent was observed at 0 V in the presence of light. Based on the findings of LSV, 1.0 V was selected as the suitable applied voltage for the PEC based AOP removal of the selected OMPs because sufficient current density (0.16 mA cm^{-2}) was obtained at 1.0 V. The obtained photocurrent density current density of 0.16 mA cm^{-2} was comparable to the current densities (0.1–1 mA cm^{-2}) reported in the relevant literature [21,54,55] that used $BiVO_4$ based photoanodes. However, the reported light intensities used in LSV was mostly 1000 W m^{-2}, which could significantly increase the photocurrent response. The increased light intensities could be the explanation of current densities higher than 0.16 mA cm^{-2} reported in the literature. The transient photocurrent response during the removal experiment as shown in Fig. S. 4 of the supplementary information is also comparable with the value (0.16 mA cm^{-2}) obtained by the LSV characterization.

The approximate value of flat band potential (E_{fb}) and the electron donor density (N_D) of fabricated $BiVO_4$ photoanode was calculated by using the Mott-Schottky plot. The E_{fb} and N_D are important parameters to assess the charge separation efficiency not only in a photocatalyst but also in heterojunction interfaces. Mott Schottky plot was constructed by using the Eq. (5) as given below:

$$\frac{1}{C^2} = \frac{2}{e\varepsilon\varepsilon_o N_D A^2} \times \left(E_A - E_{fb} - \frac{kT}{e}\right) \quad (5)$$

In Eq. (5), the C is the capacitance at the photoanode-electrolyte interface, e is the electron charge (1.60×10^{-19} C), ε is the dielectric constant (68 for $BiVO_4$ [56]), ε_o is the permittivity of vacuum, N_D is the charge carrier density (cm^{-3}), A (m^2) is the surface area of the photoanode, E_A is the applied potential, E_{fb} is the flat band potential, k is the Boltzmann constant and T is the absolute room temperature. A Mott Schottky plot ($1/C^2$ as a function of E_A (V) vs Ag/AgCl) was constructed as shown in Fig. S. 5, N_D was calculated from the slope of the linear part of the plot and the E_{fb} was determined by extrapolating the straight tangent line of the linear part of the plot to x-axis intercept as shown in Fig. S. 5 in supplementary information. The calculated value of N_D was 1.04×10^{23} cm^{-3} which was in agreement with the value reported in the literature [22] for the $BiVO_4$ photoanode used in water treatment. The approximate value of E_{fb} from the Mott Schottky plot was −0.534 V vs Ag/AgCl (0.088 V vs RHE), which also closely matched to the values reported in the literature [22]. The value of E_{fb} was consistent with the literature [22], where similar values of E_g, E_{CB} and E_{VB} were calculated by the UV–vis absorbance data and Eqs. (3) and (4).

To assess the quantum efficiency of the $BiVO_4$ photoanode, incident photon to current conversion efficiency (IPCE) characterization was carried out. It calculated the number of incoming photons that were converted into electrons by the $BiVO_4$ layer. Fig. 4 (d) shows the IPCE plot of the fabricated $BiVO_4$ photoanode and it is evident from the plot that the photoanode absorbed the incoming photons between 300 and 500 nm and converted them into photocurrent. The percentage of converted incoming photons to photocurrent at each wavelength varied, and a maximum IPCE of 9.23% was reached at 450 nm. The overall shape of IPCE plot is similar to the absorbance pattern shown in Fig. 4 (a), both the absorbance edge and the maximum IPCE were observed in the visible range (λ>400 nm) of the solar spectrum. The position of maximum IPCE in the visible range of solar spectrum (λ>400 nm) provides further evidence that dip-coating was successful in preparing a

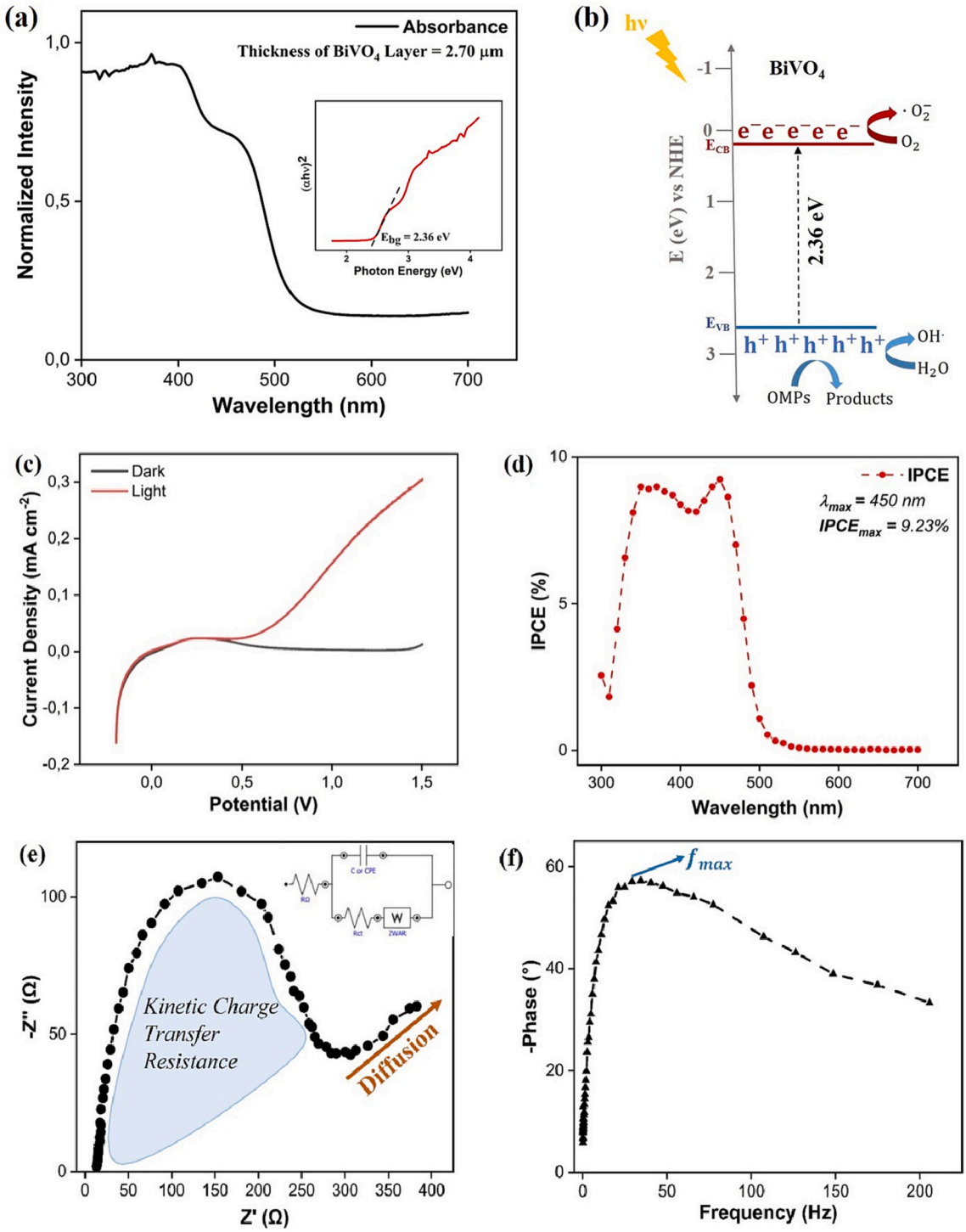

Fig. 4. (a) UV–Vis absorbance spectrum showing the absorbance pattern and the range of absorbance of the $BiVO_4$ photoanode (b) Illustration of interaction of solar photons with the $BiVO_4$ photoanode for the in-situ generation of oxidants (c) LSV plot of $BiVO_4$ photoanode under dark and light (60 W m^{-2}) conditions measured within the potential window of −0.2 to 1.5 V with a scan rate 100 mV s^{-1} (d) IPCE plot of $BiVO_4$ photoanode under 1 sun standard illumination and 1 V applied potential vs platinum wire as a counter electrode (e) Nyquist plot of $BiVO_4$ photoanode under illuminated conditions (60 W m^{-2}) performed between 10,000 Hz to 0.01 Hz at a perturbation voltage of 0.2 V (f) Bode phase angle plot showing the phase angle response to the applied frequency for electron lifetime determination.

visible light absorbing $BiVO_4$ photoanode. The short circuit current (J_{sc}) of 4.60 A m^{-2} was also obtained by the IPCE characterization that represented the maximum current that can be generated by the $BiVO_4$ photoanode..

Electrochemical impedance spectroscopy (EIS) was carried out as described in Section 2.3 to analyse the charge transfer dynamics at the photoanode-electrolyte interface. Fig. 4 (e) shows the Nyquist plot along with the equivalent circuit model that shows important elements in the circuit such as solution resistance (R), double layer capacitance (C or CPE), charge transfer resistance (R_{ct}) and Warburg diffusion coefficient (W). Among these elements, R_{ct} is the most important one as it substantially influences the reaction kinetics. The radius of the arc in the Nyquist plot is indicative of R_{ct}, with a smaller arc radius corresponding to a lower R_{ct} [44]. The calculated value of R_{ct} in Fig. 4 (e) was 142 Ω,

which was comparable to, or even smaller than, most of the values (300 Ω [44], 20,426 Ω [57] and 106 Ω [58]) reported in the literature for various photo-electrochemical applications using $BiVO_4$ based photoanodes. This inferred that the dip-coating method was successful in fabricating photoanodes with good interfacial charge transfer efficiency. The overall shape of the Nyquist plot in Fig. 4 (e) suggested that the removal rate of the OMPs in the solution was partially diffusion controlled because the tail at the end of the arc is approximately at an angle of 45° with the X-axis. This kind of shape is characteristic of mixed kinetic-diffusion controlled reactions in which the reaction rate is not only hindered by the charge transfer resistance at the electrode-electrolyte interface but also by the transport of molecules from the bulk towards the photoanode-electrolyte interface. The EIS data was also analysed with a bode phase angle plot (Fig. 4 (f)) to compute the lifetime of photo-generated electrons in the photoanode. The Bode plot relates the lifetime of the electrons with the maximum phase angle frequency of the response signal as follows [22]:

$$\tau_e = \frac{1}{2\pi f_{max}} \tag{6}$$

where τ_e is the lifetime of the electrons and f_{max} is the frequency at the maximum phase angle in the bode plot. According to Fig. 4 (f) f_{max} was 34.3 Hz, by substituting the value of f_{max} in Eq. (6) the lifetime of the photogenerated electrons was assessed to be 4.6 ms. The calculated lifetime of electrons was about 14 times higher than the lifetime reported in the literature [22], higher lifetime of electrons implied lower recombination of charge carriers in the photoanode, which will ultimately increase the removal efficiency. The increased lifetime of the photogenerated electrons was attributed to the porous structure of the $BiVO_4$ particles as discussed in Section 3.1. This porous structure reduced the internal resistance for the electron mobility within the $BiVO_4$ layer and increased the charge separation efficiency.

3.3. Photoelectrocatalytic based AOP removal of OMPs

Fig. 5 (a) shows the normalized simultaneous decrease in concentration of ACT, BTA and PRO each having an initial concentration of 45 μg L^{-1} as a result of photolysis. It is evident from Fig. 5 (a) that <10% of each OMP was removed as a result of the direct exposure of the reaction solution to the incoming simulated solar light. This low removal by photolysis is in accordance with the absorbance properties of ACT, BTA and PRO as all three OMPs absorb majorly in the UV range below 280 nm [38,47,59,60]. Photolysis results confirmed that removal of the selected OMPs was due of the use of the $BiVO_4$ photoanode for PEC advanced oxidation. Fig. S. 6 (a) in supplementary information shows the normalized simultaneous removal of the selected OMPs in the

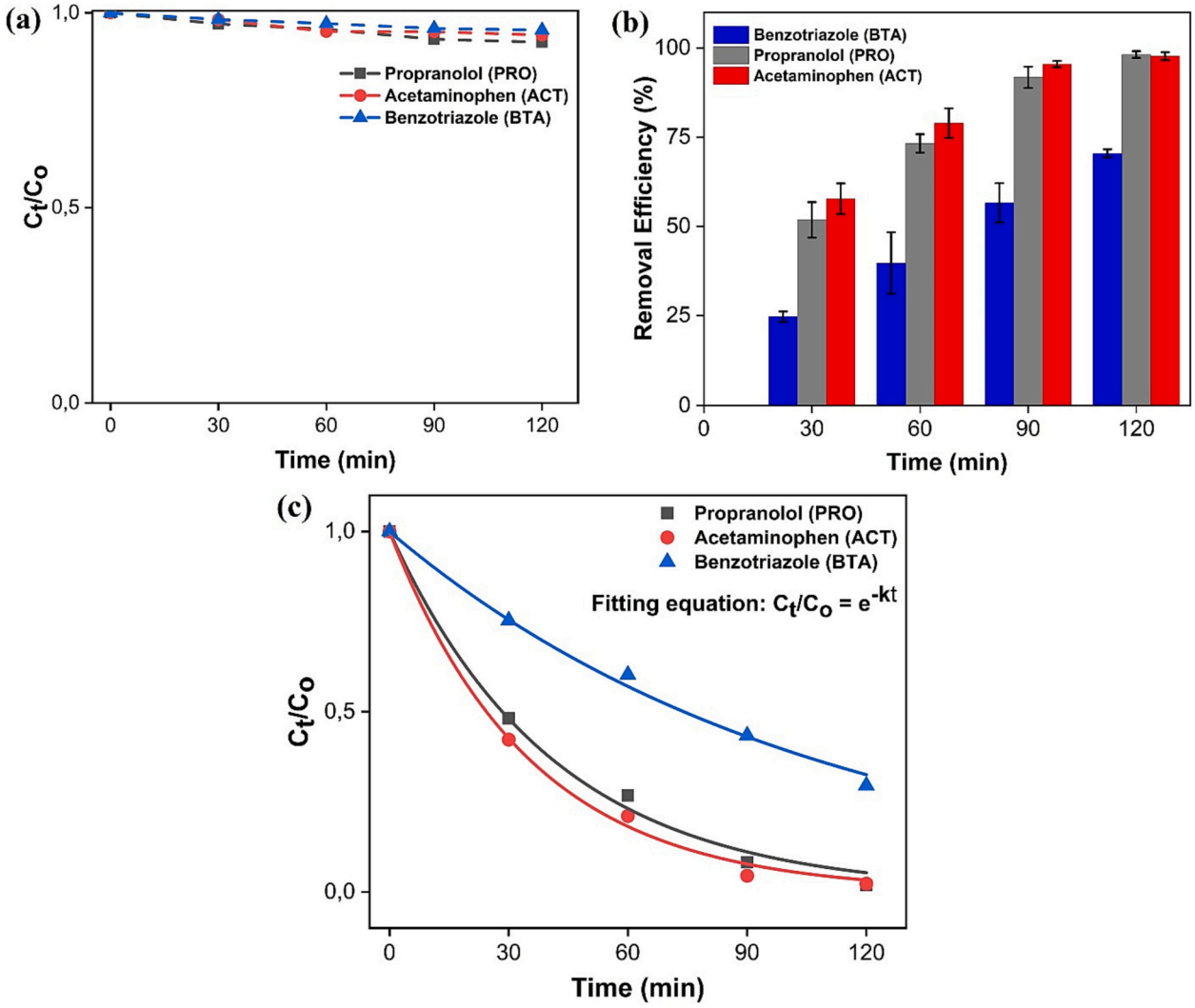

Fig. 5. (a) Normalized removal of ACT, BTA and PRO in response to direct interaction of the incoming solar simulated light (60 W m^{-2}) with the reaction solution for 2 h (b) Comparison of efficiency of removing ACT, BTA and PRO by using the $BiVO_4$ photoanode at intervals of 30 min (c) Fitting of the first order kinetic model to the normalized simultaneous removal efficiencies of ACT, BTA and PRO under illuminated condition (60 W m^{-2}) during a 120 min removal experiment.

absence of light (dark conditions) by using the fabricated $BiVO_4$ photoanode at an applied voltage of 1 V vs Ag/AgCl. It is evident from Fig. S. 6 (a) in the supplementary information that in the absence of light there was minimum removal (<15%) of OMPs confirming that the removal of OMPs was due to PEC effect. Similarly, Fig. S. 6 (b) in supplementary information shows the normalized simultaneous removal of ACT, BTA and PRO in the presence of light (60 W m^{-2}) by using the $BiVO_4$ photoanode at an applied voltage of 1 V vs Ag/AgCl. Before starting of the photo-electrocatalytic removal, 45 min of adsorption time was given to analyse the effect of OMPs adsorption by the reactor cell components (photoanode, reference electrode and counter electrode). Fig. S. 3(b) shows that under dark conditions, <10% removal of OMPs were removed through adsorption. This low removal of OMPs through adsorption suggests that the selected OMPs removal occurred due to the PEC effect. Fig. S. 5 (b) in supplementary information shows 99% removal of ACT and PRO within 2 h while approximately 70% BTA was removed after 2 h of solar simulated irradiation. Fig. 5 (b) gives more detailed information regarding the removal efficiency of photoanode for ACT, BTA and PRO on a 30 min interval basis. It shows that >50% of ACT and PRO was removed by the $BiVO_4$ photoanode within 30 min of irradiation, while only 24% of BTA was removed within 30 min of irradiation. After 30 min, the rate of removal decreased for ACT and PRO, which could have been caused by a limiting transport of ACT and PRO molecules from the bulk solution to the photoanode-electrolyte interface where the removal reaction takes place [61]. As the transport of ACT and PRO molecules towards the surface of the $BiVO_4$ photoanode became slower, the removal rate decreased, which resulted in longer times to reach 99% removal efficiencies for ACT and PRO. This observation is in agreement with the findings from the Nyquist plot (Fig. 4 (e)), showing mixed kinetic-diffusion for the removal of ACT. The decrease in (normalized) concentration of BTA remained almost constant after 30 min, suggesting that the BTA removal was not influenced by the limiting transport of molecules towards the surface of photoanode. The low removal efficiency of $BiVO_4$ photoanode for BTA in comparison to ACT and PRO was most likely due to its low reactivity with •OH. The reactivity of •OH is influenced by the presence of functional groups and the chemical structure of the compound under consideration. BTA is generally resistant to oxidation by •OH because the triazole ring in BTA is relatively stable and cannot be easily oxidized by •OH attack, whereas the N—H bond and the aromatic ring in BTA are more prone to •OH attack for oxidation [29]. In the case of PRO, the presence of primary and secondary alcohol groups makes it highly reactive to oxidation by •OH. Moreover, the aromatic ring in PRO could also be oxidized by •OH which can further enhance the kinetics of PRO removal [62]. Similarly in ACT, the phenolic hydroxyl and the amide group are highly susceptible to oxidation by •OH, which results in its fast removal [63]. Overall, it is likely that ACT and PRO involved more reaction pathways as compared to BTA for the oxidation by •OH due to their chemical structure and attached functional groups that resulted in their higher removal. The complete reaction pathway and the ultimate fate of ACT, BTA and PRO in demineralized water could not be confirmed in this study because the intermediate products were not analysed. The identification and quantification of intermediate products of OMPs are quite challenging because of the low initial concentration of parent OMP in the reaction solution [64]. Moreover, analysing the intermediate products of more than one OMP in a solution is complex [65] and was beyond the scope of this study.

The kinetics of PEC based simultaneous removal of ACT, BTA and PRO during 2 h of solar simulated irradiation is shown in Fig. 5 (c). A first order rate equation ($C_t/C_0=e^{-kt}$) was used to compute the rate coefficients of ACT, BTA and PRO removal because the normalized decrease matched the first order kinetic model. As expected, the rate coefficients of ACT and PRO were almost equal (Table 1) and about 67% higher than the rate coefficient of BTA. Similarly, the half-life times of PEC based simultaneous removal of ACT and PRO were also approximately 67% higher than the half-life of BTA. Rate coefficients given in Table 1 are similar and comparable to the previous studies using different AOPs for the removal of ACT [66,67], BTA [68] and PRO [62] having initial concentrations of >1 mg L^{-1}. Table 2 summarizes a comparison between the removal efficiency of the fabricated $BiVO_4$ photoanode used in this study with the relevant literature is presented in Table 2. According to Table 2 most of the literature studies used 1.0 V as the applied external voltage, but the resulting removal efficiencies are lower than the removal efficiency of the $BiVO_4$ photoanode used in this study.

Table 1
Rate coefficients of first order reaction kinetics along with R^2 values and half-life times of ACT, BTA and PRO after 2 h of removal experiment by using $BiVO_4$ photoanode.

	Rate Coefficient (min^{-1})	R^2	Half-life time (min)
Acetaminophen	2.84×10^{-2}	0.993	28
Propranolol	2.44×10^{-2}	0.994	24
Benzotriazole	9.35×10^{-3}	0.996	74

The results of the reusability experiments are shown in Fig. S. 7 of supplementary information. In reusability experiments, a $BiVO_4$ photoanode was used for four consecutive experiments of 2 h each. The $BiVO_4$ photoanode showed good reusability performance as the removal efficiency was only 17, 22 and 32% decreased for ACT, BTA and PRO respectively after three consecutive experiments of using one and the same photoanode. After the second experiment the removal efficiency of the photoanode remained constant as shown in supplementary information Fig. S. 7, the decrease in efficiency was most likely due to the adsorption of the unoxidized OMP molecules within the surface cracks of the photoanode that decreased the active surface area available for the water oxidation to produce reactive species (•OH and $^{\bullet}O_2^-$).

3.3.1. Electrical energy per order

The electrical energy per order (E_{EO}) quantifies the energy required (electrical and solar) in kilowatt hours (kWh) to decrease the concentration of an OMP in 1 m^3 volume of water by a factor of 10 (1 log reduction). E_{EO} for the selected OMPs was calculated by using Eq. (7) below [74]:

$$E_{EO} = \frac{P \times t \times 1000}{V \times 60 \times log\left(\frac{C_i}{C_f}\right)} \quad (7)$$

where P (kW) is the total input power, t (min) is the reaction time for the OMP removal, V (L) is the treated volume, C_i and C_f are initial and final concentrations of the OMP, respectively. For a first order reaction the term $\log(C_i/C_f)$ equals 0.4343kt, therefore, the final simplified E_{EO} equation is given below in Eq. (8) [75]:

$$E_{EO} = \frac{38.4 \times P}{V \times k} \quad (8)$$

In Eq. (6), k (min^{-1}) is the rate coefficient of the OMPs given in Table 1. Variable P (kW) is the total input power including electrical power and irradiation power that is available for the absorption by the $BiVO_4$ photoanode within its total absorbance area (300–550 nm). The total light intensity measured by a photodiode between 300 and 550 nm for 16 cm^2 surface area of photoanode was 1.09×10^{-3} kW. The applied electrical power was 1.6×10^{-6} kW based on 1 V external bias and 1.6 mA photocurrent. Therefore, the total input power of the system was 1.0916×10^{-3} kW, the E_{EO} values for each OMP are given in Fig. 6 (a) by substituting the values of V (0.167 L), P (1.0916×10^{-3} kW) and rate coefficients (k) in Eq. (8). The E_{EO} value for BTA in Fig. 6 (a) is higher than the E_{EO} values of ACT and PRO due to its slow removal kinetics. The total energy consumption (including both light intensity and electrical power) of the removal process of 2 h was calculated as 13.07 kWh m^{-3}.

Table 2
Summary table showing the comparison between the removal efficiency of the $BiVO_4$ photoanode used in this study with the relevant literature studies.

Photoanode	Pollutant compound	Applied potential and light intensity	Removal efficiency	Ref
$BiVO_4$	Acetaminophen, Benzotriazole and Propranolol each at a starting concentration of 45 μg L^{-1}	1 V vs Ag/AgCl and 60 W m^{-2} light intensity (calibrated between 300 and 400 nm)	Simultaneous Removal of Acetaminophen 99%, Propranolol 100% and Benzotriazole 70% in 120 min	This Study
$BiVO_4$	Methylene Blue at 10 mg L^{-1}	1.0 V vs Ag/AgCl and 100 mW cm^{-2} of light intensity	50% in 80 min	[69]
$BiVO_4$	Ciprofloxacin at 10 mg L^{-1}	1.0 V vs Ag/AgCl and 100 mW cm^{-2} of light intensity	50% in 120 min	[22]
WO_3/ $BiVO_4$@FeOOH	Sulfamethoxazole at 25 mg L^{-1}	1.0 vs RHE and light intensity of 100 mW cm^{-2}	35% in 120 min	[70]
$BiVO_4$	Phenol at 20 mg L^{-1}	1.0 vs Ag/AgCl and light intensity of 60 W m^{-2}	65% in 240 min	[71]
$BiVO_4$/TiO_2 nanotube	Tetracycline hydrochloride at 10 mg L^{-1}	0 V and light intensity of 100 mW cm^{-2}	23% in 120 min	[72]
$BiVO_4$/WO_3	Norfloxaxin at 10 mg L^{-1}	1.0 V vs SCE and light intensity of 1 mW cm^{-1}	63% in 180 min	[73]

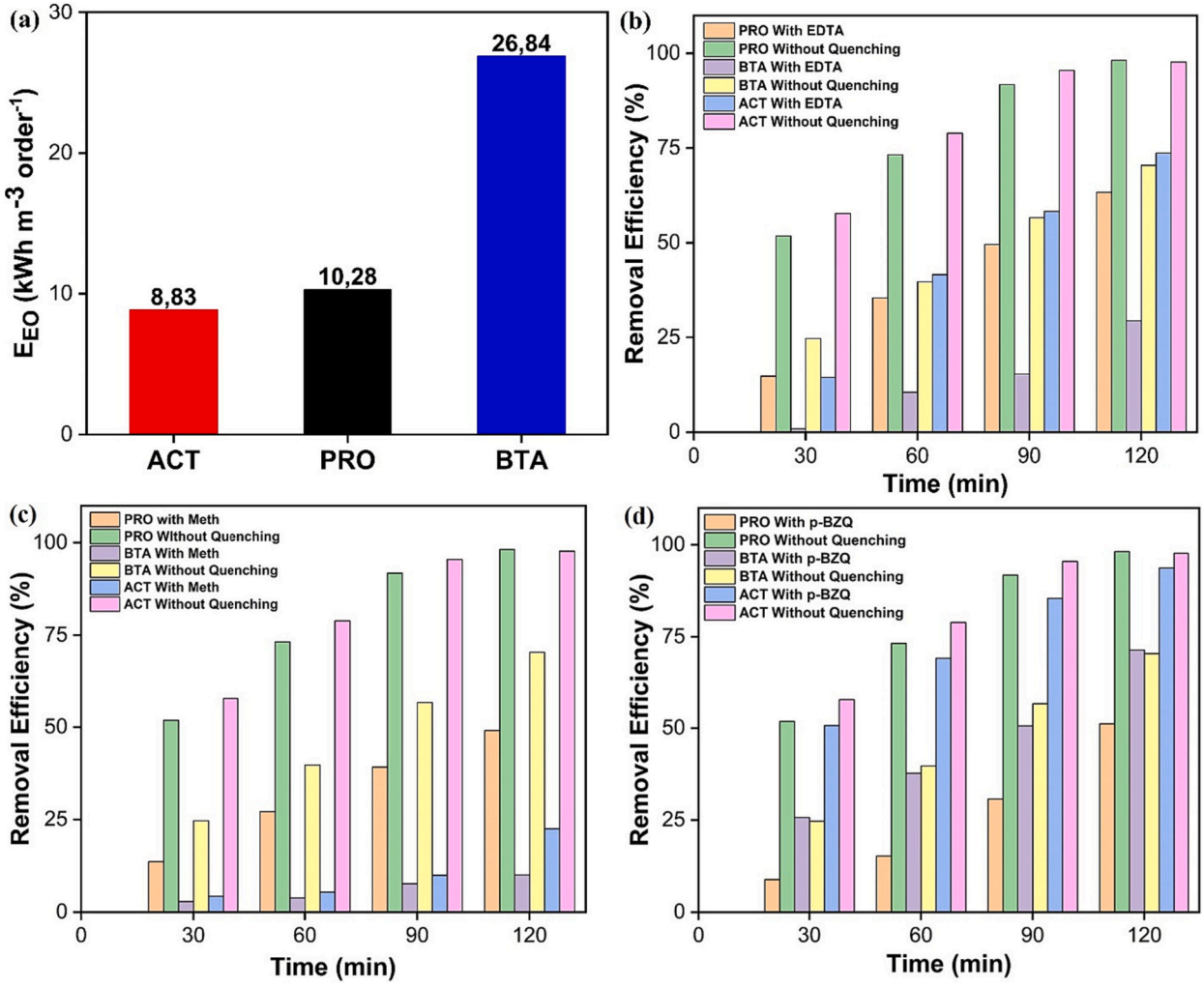

Fig. 6. (a) E_{EO} values for the complete removal of ACT, BTA and PRO (b) Removal efficiency of $BiVO_4$ photoanode for the removal of ACT, BTA and PRO in the presence of 4 mM EDTA, (c) 4 mM methanol and (d) 4 mM p-BZQ as quenching agents.

3.3.2. *Quenching of reactive species*

Quenching experiments were performed by using $BiVO_4$ photoanodes for the simultaneous removal of the selected OMPs in the presence of a quenching agent. EDTA, methanol and p-BZQ were used in separate experiments to quench photogenerated holes, hydroxyl and super-oxide radicals, respectively. Fig. 6 (b), (c) and (d) show the removal efficiency of $BiVO_4$ photoanode for the selected OMPs in the presence of selected quenching agents. In the presence of EDTA (Fig. 6 (b)), the removal efficiency of all OMPs decreased but the most pronounced effect was observed for BTA where the removal efficiency decreased from 70% (without quenching) to 29%. This substantial decrease in the removal of BTA suggested that photogenerated holes have the potential to directly oxidize the BTA molecules at the surface of the $BiVO_4$ photoanode. EDTA quenched the photogenerated holes thereby decreasing the in-situ generation of •OH, which could be another explanation for the decrease in the removal of all three OMPs because less •OH would be available for the oxidation. In the presence of methanol, all three OMPs showed substantial decrease in the removal

efficiency as shown in Fig. 6 (c). The decrease in the removal efficiency of ACT and BTA was higher compared to PRO which implies that •OH were the dominating reactive species for ACT and BTA. In the presence of p-BZQ, the removal efficiency of PRO decreased (Fig. 6 (d)) from 98% (without quenching) to 51%, whereas negligible decrease in the removal efficiency of ACT and BTA was observed. The substantial decrease in the removal efficiency of all three OMPs in the presence of methanol suggested that •OH were the dominating reactive specie for the oxidation of all three OMPs. Similarly, the quenching results exhibited that the oxidation of PRO and BTA was partially influenced by $^{\bullet}O_2^-$ and photogenerated holes, respectively.

4. Conclusions

A $BiVO_4$ photoanode was successfully fabricated by using a simple and effective dip-coating method to deposit a $BiVO_4$ photocatalytic layer on FTO glass slides. SEM characterization showed a rough surface morphology of the fabricated photoanode that was favourable for the adsorption of OMP molecules. The rough and porous surface morphology of the $BiVO_4$ photoanode played an important role for the generation of reactive species at the photoanode-electrolyte interface. Similarly, UV–Vis spectroscopy and IPCE measurements confirmed that the fabricated photoanode absorbed light in the visible spectrum of the solar irradiation for the in-situ generation of oxidants. The dip-coated $BiVO_4$ photoanode, used in the PEC-based AOP removal, simultaneously removed >70% of the selected OMPs from the solution after 2 h. However, during the simultaneous removal, ACT and PRO showed faster removal kinetics than BTA. The faster removal of ACT and PRO was most likely due to their chemical structures and the presence of functional groups that facilitate multiple oxidation pathways for the attack of reactive species at the photoanode-electrolyte interface. Consequently, BTA required about 67% more energy for its removal from the solution than ACT and PRO. Findings of the quenching study revealed that •OH radicals were the dominating reactive species in our research for the PEC based simultaneous oxidation of the selected OMPs. The results obtained in this study are promising and could be considered as a foundation step towards the PEC-based simultaneous removal of multiple OMPs in WWTP effluents.

Declaration of competing interest

The authors declare that they have no known competing financial interests or personal relationships that could have appeared to influence the work reported in this paper.

Data availability

Data will be made available on request.

Acknowledgement

This research study was financed under the InnovEOX project that has received funding from the European Union's EU Framework Programme for Research and Innovation Horizon 2020 under Grant Agreement No 861369.

Appendix A. Supplementary data

Supplementary data to this article can be found online at https://doi.org/10.1016/j.jwpe.2023.104471.

References

[1] M.V. Pablos, P. García-Hortigüela, C. Fernández, Acute and chronic toxicity of emerging contaminants, alone or in combination, in *Chlorella vulgaris* and *Daphnia magna*, Environ Sci Pollut Res. 22 (2015) 5417–5424, https://doi.org/10.1007/s11356-015-4119-1.

[2] M.O. Barbosa, N.F.F. Moreira, A.R. Ribeiro, M.F.R. Pereira, A.M.T. Silva, Occurrence and removal of organic micropollutants: an overview of the watch list of EU decision 2015/495, Water Res. 94 (2016) 257–279, https://doi.org/10.1016/j.watres.2016.02.047.

[3] E.M.M. Wanda, H. Nyoni, B.B. Mamba, T.A.M. Msagati, Application of silica and germanium dioxide nanoparticles/ polyethersulfone blend membranes for removal of emerging micropollutants from water, Phys. Chem. Earth A/B/C. 108 (2018) 28–47, https://doi.org/10.1016/j.pce.2018.08.004.

[4] T. Rasheed, M. Bilal, F. Nabeel, M. Adeel, H.M.N. Iqbal, Environmentally-related contaminants of high concern: potential sources and analytical modalities for detection, quantification, and treatment, Environ. Int. 122 (2019) 52–66, https://doi.org/10.1016/j.envint.2018.11.038.

[5] M. Hecker, H. Hollert, Endocrine disruptor screening: regulatory perspectives and needs, Environ. Sci. Eur. 23 (2011) 15, https://doi.org/10.1186/2190-4715-23-15.

[6] E. Neczaj, A. Grosser, Circular Economy in Wastewater Treatment Plant–Challenges and Barriers, Proceedings 2, 2018, p. 614, https://doi.org/10.3390/proceedings2110614.

[7] A. Chavoshani, M. Hashemi, M. Mehdi Amin, S.C. Ameta, Chapter 1 - introduction, in: A. Chavoshani, M. Hashemi, M. Mehdi Amin, S.C. Ameta (Eds.), Micropollutants and Challenges, Elsevier, 2020, pp. 1–33, https://doi.org/10.1016/B978-0-12-818612-1.00001-5.

[8] Z.A. Yacouba, J. Mendret, G. Lesage, F. Zaviska, S. Brosillon, Removal of organic micropollutants from domestic wastewater: the effect of ozone-based advanced oxidation process on nanofiltration, J. Water Process Eng. 39 (2021), 101869, https://doi.org/10.1016/j.jwpe.2020.101869.

[9] Y. Dubowski, Y. Alfiya, Y. Gilboa, S. Sabach, E. Friedler, Removal of organic micropollutants from biologically treated greywater using continuous-flow vacuum-UV/UVC photo-reactor, Environ. Sci. Pollut. Res. 27 (2020) 7578–7587, https://doi.org/10.1007/s11356-019-07399-7.

[10] S. Garcia-Segura, E. Brillas, Applied photoelectrocatalysis on the degradation of organic pollutants in wastewaters, J. Photochem. Photobiol. C Photchem. Rev. 31 (2017) 1–35, https://doi.org/10.1016/j.jphotochemrev.2017.01.005.

[11] B.O. Orimolade, O.A. Arotiba, Bismuth vanadate in photoelectrocatalytic water treatment systems for the degradation of organics: a review on recent trends, J. Electroanal. Chem. 878 (2020), 114724, https://doi.org/10.1016/j.jelechem.2020.114724.

[12] T.A. Aragaw, F.M. Bogale, B.A. Aragaw, Iron-based nanoparticles in wastewater treatment: a review on synthesis methods, applications, and removal mechanisms, J. Saudi Chem. Soc. 25 (2021), 101280, https://doi.org/10.1016/j.jscs.2021.101280.

[13] M.C. Collivignarelli, A. Abbà, M. Carnevale Miino, G. Bertanza, S. Sorlini, S. Damiani, H. Arab, M. Bestetti, S. Franz, Photoelectrocatalysis on TiO2 meshes: different applications in the integrated urban water management, Environ. Sci. Pollut. Res. 28 (2021) 59452–59461, https://doi.org/10.1007/s11356-021-12606-5.

[14] M. Liao, L. Su, Y. Deng, S. Xiong, R. Tang, Z. Wu, C. Ding, L. Yang, D. Gong, Strategies to improve WO3-based photocatalysts for wastewater treatment: a review, J. Mater. Sci. 56 (2021) 14416–14447, https://doi.org/10.1007/s10853-021-06202-8.

[15] S. Rajeswari, R. Venckatesh, Chapter 24 - ZnO-based nanoparticles for wastewater treatment: A review, in: K.A. Abd-Elsalam (Ed.), Zinc-Based Nanostructures for Environmental and Agricultural Applications, Elsevier, 2021, pp. 485–507, https://doi.org/10.1016/B978-0-12-822836-4.00022-7.

[16] D.T. Sponza, R. Oztekin, Treatment of olive mill wastewater by photooxidation with ZrO2-doped TiO2 nanocomposite and its reuse capability, Environ. Technol. 37 (2016) 865–879, https://doi.org/10.1080/09593330.2015.1088579.

[17] H. Shao, Y. Wang, H. Zeng, J. Zhang, Y. Wang, M. Sillanpää, X. Zhao, Enhanced photoelectrocatalytic degradation of bisphenol a by BiVO4 photoanode coupling with peroxymonosulfate, J. Hazard. Mater. 394 (2020), 121105, https://doi.org/10.1016/j.jhazmat.2019.121105.

[18] T. Ahmed, M. Ammar, A. Saleem, H. Zhang, H. Xu, Z-scheme 2D-m-BiVO4 networks decorated by a g-CN nanosheet heterostructured photocatalyst with an excellent response to visible light, RSC Adv. 10 (2020) 3192–3202, https://doi.org/10.1039/C9RA09473C.

[19] B. Samran, S. Lunput, S. Tonnonchiang, S. Chaiwichian, BiFeO3/BiVO4 nanocomposite photocatalysts with highly enhanced photocatalytic activity for rhodamine B degradation under visible light irradiation, Phys. B Condens. Matter 561 (2019) 23–28, https://doi.org/10.1016/j.physb.2019.02.049.

[20] H. Jiang, H. Dai, X. Meng, L. Zhang, J. Deng, K. Ji, Morphology-dependent photocatalytic performance of monoclinic BiVO4 for methyl Orange degradation under visible-light irradiation, Chin. J. Catal. 32 (2011) 939–949, https://doi.org/10.1016/S1872-2067(10)60215-X.

[21] L. Xia, J. Li, J. Bai, L. Li, Q. Zeng, Q. Xu, B. Zhou, Preparation of a BiVO4 nanoporous photoanode based on peroxovanadate reduction and conversion for efficient photoelectrochemical performance, Nanoscale 10 (2018) 2848–2855, https://doi.org/10.1039/C7NR07566A.

[22] B.O. Orimolade, O.A. Arotiba, Towards visible light driven photoelectrocatalysis for water treatment: application of a FTO/BiVO4/Ag2S heterojunction anode for the removal of emerging pharmaceutical pollutants, Sci. Rep. 10 (2020) 5348, https://doi.org/10.1038/s41598-020-62425-w.

[23] C. Regmi, Y.K. Kshetri, T.-H. Kim, R.P. Pandey, S.K. Ray, S.W. Lee, Fabrication of Ni-doped BiVO4 semiconductors with enhanced visible-light photocatalytic performances for wastewater treatment, Appl. Surf. Sci. 413 (2017) 253–265, https://doi.org/10.1016/j.apsusc.2017.04.056.

[24] B.O. Orimolade, B.A. Koiki, B.N. Zwane, G.M. Peleyeju, N. Mabuba, O.A. Arotiba, Interrogating solar photoelectrocatalysis on an exfoliated graphite–BiVO4/ZnO composite electrode towards water treatment, RSC Adv. 9 (2019) 16586–16595, https://doi.org/10.1039/C9RA02366F.
[25] P. Perez-Rodriguez, Y. Bennani, M.J. Alani, W. Smith, L.C. Rietveld, M. Zeman, A. H.M. Smets, Treatment of organic pollutants using a solar energy driven photo-oxidation device, Adv. Sustain. Syst. 1 (2017) 1700010, https://doi.org/10.1002/adsu.201700010.
[26] R. Loos, B.M. Gawlik, G. Locoro, E. Rimaviciute, S. Contini, G. Bidoglio, EU-wide survey of polar organic persistent pollutants in European river waters, Environ. Pollut. 157 (2009) 561–568, https://doi.org/10.1016/j.envpol.2008.09.020.
[27] H.-G. Ni, F.-H. Lu, X.-L. Luo, H.-Y. Tian, E.Y. Zeng, Occurrence, phase distribution, and mass loadings of Benzothiazoles in riverine runoff of the Pearl River Delta, China, Environ. Sci. Technol. 42 (2008) 1892–1897, https://doi.org/10.1021/es071871c.
[29] N.K. Vel Leitner, B. Roshani, Kinetic of benzotriazole oxidation by ozone and hydroxyl radical, Water Res. 44 (2010) 2058–2066, https://doi.org/10.1016/j.watres.2009.12.018.
[30] A.A. Mazioti, A.S. Stasinakis, G. Gatidou, N.S. Thomaidis, H.R. Andersen, Sorption and biodegradation of selected benzotriazoles and hydroxybenzothiazole in activated sludge and estimation of their fate during wastewater treatment, Chemosphere 131 (2015) 117–123, https://doi.org/10.1016/j.chemosphere.2015.03.029.
[31] E. Borowska, E. Felis, J. Kalka, Oxidation of benzotriazole and benzothiazole in photochemical processes: kinetics and formation of transformation products, Chem. Eng. J. 304 (2016) 852–863, https://doi.org/10.1016/j.cej.2016.06.123.
[32] N.H.S. Javadi, M. Baghdadi, N. Mehrdadi, M. Mortazavi, Removal of benzotriazole from secondary municipal wastewater effluent by catalytic ozonation in the presence of magnetic alumina nanocomposite, Journal of Environmental, Chem. Eng. 6 (2018) 6421–6430, https://doi.org/10.1016/j.jece.2018.09.063.
[33] J. Xu, L. Li, C. Guo, Y. Zhang, S. Wang, Removal of benzotriazole from solution by BiOBr photocatalysis under simulated solar irradiation, Chem. Eng. J. 221 (2013) 230–237, https://doi.org/10.1016/j.cej.2013.01.081.
[34] M.J. Elman, J. Sugar, R. Fiscella, T.A. Deutsch, J. Noth, M. Nyberg, K. Packo, R. J. Anderson, The effect of propranolol versus placebo on resident surgical performance, Trans. Am. Ophthalmol. Soc. 96 (1998) 283–294.
[35] M. Petrović, B. Škrbić, J. Živančev, L. Ferrando-Climent, D. Barcelo, Determination of 81 pharmaceutical drugs by high performance liquid chromatography coupled to mass spectrometry with hybrid triple quadrupole–linear ion trap in different types of water in Serbia, Sci. Total Environ. 468–469 (2014) 415–428, https://doi.org/10.1016/j.scitotenv.2013.08.079.
[36] Q. Zheng, D.K. Unruh, K.M. Hutchins, Removal of the micropollutants propranolol hydrochloride and 2-naphthol from water by pyridine-functionalized polymers, Front. Chem. 9 (2022). https://www.frontiersin.org/articles/10.3389/fchem.2021.793870. (Accessed 20 March 2023).
[37] Y. Somasundar, L.Q. Shen, A.G. Hoane, L.L. Tang, M.R. Mills, A.E. Burton, A. D. Ryabov, T.J. Collins, Structural, mechanistic, and ultradilute catalysis portrayal of substrate inhibition in the TAML–hydrogen peroxide catalytic oxidation of the persistent drug and micropollutant, propranolol, J. Am. Chem. Soc. 140 (2018) 12280–12289, https://doi.org/10.1021/jacs.8b08108.
[38] T. Giordani, J. Dose, Y. Kuskoski, J. Schultz, A.S. Mangrich, J.M.M. de Mello, L. L. Silva, R.C.F. Zeferino, M. Zanetti, M.A. Fiori, G.L. Colpani, Photocatalytic degradation of propranolol hydrochloride using Nd–TiO2 nanoparticles under UV and visible light, J. Mater. Res. 36 (2021) 1584–1599, https://doi.org/10.1557/s43578-021-00207-4.
[39] H. Nsubuga, C. Basheer, A. Jalilov, M.B. Haider, A.A. Al-Saadi, Droplet flow-assisted heterogeneous electro-Fenton reactor for degradation of beta-blockers: response surface optimization, and mechanism elucidation, Environ. Sci. Pollut. Res. 26 (2019) 14313–14327, https://doi.org/10.1007/s11356-019-04551-1.
[40] H.N. Phong Vo, G.K. Le, T.M. Hong Nguyen, X.-T. Bui, K.H. Nguyen, E.R. Rene, T. D.H. Vo, N.-D. Thanh Cao, R. Mohan, Acetaminophen micropollutant: historical and current occurrences, toxicity, removal strategies and transformation pathways in different environments, Chemosphere 236 (2019), 124391, https://doi.org/10.1016/j.chemosphere.2019.124391.
[41] M. Sajid, S. Bari, M. Saif Ur Rehman, M. Ashfaq, Y. Guoliang, G. Mustafa, Adsorption characteristics of paracetamol removal onto activated carbon prepared from Cannabis sativum hemp, Alex. Eng. J. 61 (2022) 7203–7212, https://doi.org/10.1016/j.aej.2021.12.060.
[42] W.J. Lee, P.S. Goh, W.J. Lau, A.F. Ismail, Removal of pharmaceutical contaminants from aqueous medium: a state-of-the-art review based on paracetamol, Arab. J. Sci. Eng. 45 (2020) 7109–7135, https://doi.org/10.1007/s13369-020-04446-1.
[43] Y. Ouarda, Electro-oxidation of secondary effluents from various wastewater plants for the removal of acetaminophen and dissolved organic matter, Sci. Total Environ. 8 (2020).
[44] B.O. Orimolade, B.A. Koiki, G.M. Peleyeju, O.A. Arotiba, Visible light driven photoelectrocatalysis on a FTO/BiVO4/BiOI anode for water treatment involving emerging pharmaceutical pollutants, Electrochim. Acta 307 (2019) 285–292, https://doi.org/10.1016/j.electacta.2019.03.217.
[45] B. Quinn, F. Gagné, C. Blaise, Evaluation of the acute, chronic and teratogenic effects of a mixture of eleven pharmaceuticals on the cnidarian, Hydra attenuata, Sci. Total Environ. 407 (2009) 1072–1079, https://doi.org/10.1016/j.scitotenv.2008.10.022.
[46] M. Ijaz, T. Ahmed, A. Iftikhar Ahmad, Toxic organic micropollutants and associated health impacts, in: T. Ahmed, M.Z. Hashmi (Eds.), Hazardous Environmental Micro-pollutants, Health Impacts and Allied Treatment Technologies, Springer International Publishing, Cham, 2022, pp. 205–217, https://doi.org/10.1007/978-3-030-96523-5_9.
[47] A.Z. Ali, Y. Wu, Y.-D. Bennani, H. Spanjers, J.P. van der Hoek, Photo-electrocatalytic based removal of acetaminophen: application of visible light driven heterojunction based BiVO4/BiOI photoanode, Chemosphere 324 (2023), 138322, https://doi.org/10.1016/j.chemosphere.2023.138322.
[48] S. Tokunaga, H. Kato, A. Kudo, Selective preparation of monoclinic and tetragonal BiVO4 with scheelite structure and their photocatalytic properties, Chem. Mater. 13 (2001) 4624–4628, https://doi.org/10.1021/cm0103390.
[49] S. Meng, T. Ogawa, H. Okumura, K.N. Ishihara, Enhanced photocatalytic activity of BiVO4/Bi2S3/SnS2 heterojunction under visible light, Catalysts 10 (2020) 1294, https://doi.org/10.3390/catal10111294.
[50] Y. Zhang, L. Shi, Z. Geng, T. Ren, Z. Yang, The improvement of photocatalysis O2 production over BiVO4 with amorphous FeOOH shell modification, Sci. Rep. 9 (2019) 19090, https://doi.org/10.1038/s41598-019-54940-2.
[51] T. Xia, M. Chen, L. Xiao, W. Fan, B. Mao, D. Xu, P. Guan, J. Zhu, W. Shi, Dip-coating synthesis of P-doped BiVO4 photoanodes with enhanced photoelectrochemical performance, J. Taiwan Inst. Chem. Eng. 93 (2018) 582–589, https://doi.org/10.1016/j.jtice.2018.09.003.
[52] H. Huang, C. Ma, Z. Zhu, X. Yao, Y. Liu, Z. Liu, C. Li, Y. Yan, Insights into enhanced visible light photocatalytic activity of t-Se nanorods/BiOCl ultrathin nanosheets 1D/2D heterojunctions, Chem. Eng. J. 338 (2018) 218–229, https://doi.org/10.1016/j.cej.2017.12.012.
[53] R.G. Pearson, Absolute electronegativity and hardness: application to inorganic chemistry, Inorg. Chem. 27 (1988) 734–740, https://doi.org/10.1021/ic00277a030.
[54] D.K. Zhong, S. Choi, D.R. Gamelin, Near-complete suppression of surface recombination in solar photoelectrolysis by “co-pi” catalyst-modified W:BiVO4, J. Am. Chem. Soc. 133 (2011) 18370–18377, https://doi.org/10.1021/ja207348x.
[55] H.L. Tan, R. Amal, Y.H. Ng, Alternative strategies in improving the photocatalytic and photoelectrochemical activities of visible light-driven BiVO4: a review, J. Mater. Chem. A 5 (2017) 16498–16521, https://doi.org/10.1039/C7TA04441K.
[56] S. Bai, J. Liu, M. Cui, R. Luo, J. He, A. Chen, Two-step electrodeposition to fabricate the p–n heterojunction of a Cu2O/BiVO4 photoanode for the enhancement of photoelectrochemical water splitting, Dalton Trans. 47 (2018) 6763–6771, https://doi.org/10.1039/C7DT04258B.
[57] Y. Li, X. Sun, Y. Tang, Y.H. Ng, L. Li, F. Jiang, J. Wang, W. Chen, L. Li, Understanding photoelectrocatalytic degradation of tetracycline over three-dimensional coral-like ZnO/BiVO4 nanocomposite, Mater. Chem. Phys. 271 (2021), 124871, https://doi.org/10.1016/j.matchemphys.2021.124871.
[58] S.W. Hwang, J.U. Kim, J.H. Baek, S.S. Kalanur, H.S. Jung, H. Seo, I.S. Cho, Solution-processed TiO2/BiVO4/SnO2 triple-layer photoanode with enhanced photoelectrochemical performance, J. Alloys Compd. 785 (2019) 1245–1252, https://doi.org/10.1016/j.jallcom.2019.01.251.
[59] M. Serdechnova, V.L. Ivanov, M.R.M. Domingues, D.V. Evtuguin, M.G.S. Ferreira, M.L. Zheludkevich, Photodegradation of 2-mercaptobenzothiazole and 1,2,3-benzotriazole corrosion inhibitors in aqueous solutions and organic solvents, Phys. Chem. Chem. Phys. 16 (2014) 25152–25160, https://doi.org/10.1039/C4CP03867C.
[60] R. Xiong, Z. Lu, Q. Tang, X. Huang, H. Ruan, W. Jiang, Y. Chen, Z. Liu, J. Kang, D. Liu, UV-LED/chlorine degradation of propranolol in water: degradation pathway and product toxicity, Chemosphere 248 (2020), 125957, https://doi.org/10.1016/j.chemosphere.2020.125957.
[61] P. Attri, Y.H. Kim, D.H. Park, J.H. Park, Y.J. Hong, H.S. Uhm, K.-N. Kim, A. Fridman, E.H. Choi, Generation mechanism of hydroxyl radical species and its lifetime prediction during the plasma-initiated ultraviolet (UV) photolysis, Sci. Rep. 5 (2015) 9332, https://doi.org/10.1038/srep09332.
[62] H.A. Nájera-Aguilar, R. Mayorga-Santis, R.F. Gutiérrez-Hernández, A. Santiesteban-Hernández, F.J. Rodríguez-Valadez, D.A. Ulloa-Gutiérrez, J. A. Araiza-Aguilar, A. Cruz-Salomón, Propranolol degradation through processes based on the generation of hydroxyl free radical, J. Water Health 20 (2021) 216–226, https://doi.org/10.2166/wh.2021.156.
[63] M. Qutob, M.A. Hussein, K.A. Alamry, M. Rafatullah, A review on the degradation of acetaminophen by advanced oxidation process: pathway, by-products, biotoxicity, and density functional theory calculation, RSC Adv. 12 (2022) 18373–18396, https://doi.org/10.1039/D2RA02469A.
[64] N. Singhal, O. Perez-Garcia, Degrading organic micropollutants: the next challenge in the evolution of biological wastewater treatment processes, Front. Environ. Sci. 4 (2016). https://www.frontiersin.org/articles/10.3389/fenvs.2016.00036. (Accessed 4 April 2023).
[65] E. Kudlek, A. Lempart-Rapacewicz, M. Dudziak, Identification of potential harmful transformation products of selected micropollutants in outdoor and indoor swimming pool water, Int. J. Environ. Res. Public Health 19 (2022) 5660, https://doi.org/10.3390/ijerph19095660.
[66] F. Audino, J.M. Toro Santamaria, L.J. del Valle Mendoza, M. Graells, M. Pérez-Moya, Removal of paracetamol using effective advanced oxidation processes, Int. J. Environ. Res. Public Health 16 (2019) 505, https://doi.org/10.3390/ijerph16030505.
[67] F. Ghanbari, A. Yaghoot-Nezhad, S. Wacławek, K.-Y.A. Lin, J. Rodríguez-Chueca, F. Mehdipour, Comparative investigation of acetaminophen degradation in aqueous solution by UV/chlorine and UV/H2O2 processes: kinetics and toxicity assessment, process feasibility and products identification, Chemosphere 285 (2021), 131455, https://doi.org/10.1016/j.chemosphere.2021.131455.
[68] F. Ghanbari, M. Khatebasreh, M. Mahdavianpour, K.-Y.A. Lin, Oxidative removal of benzotriazole using peroxymonosulfate/ozone/ultrasound: synergy, optimization,

degradation intermediates and utilizing for real wastewater, Chemosphere 244 (2020), 125326, https://doi.org/10.1016/j.chemosphere.2019.125326.
[69] R. Wang, J. Bai, Y. Li, Q. Zeng, J. Li, B. Zhou, BiVO4/TiO2(N2) nanotubes heterojunction photoanode for highly efficient photoelectrocatalytic applications, Nano-Micro Lett. 9 (2016) 14, https://doi.org/10.1007/s40820-016-0115-3.
[70] Z. Chi, J. Zhao, Y. Zhang, H. Yu, H. Yu, Coral-like WO3/BiVO4 photoanode constructed via morphology and facet engineering for antibiotic wastewater detoxification and hydrogen recovery, Chem. Eng. J. 428 (2022), 131817, https://doi.org/10.1016/j.cej.2021.131817.
[71] Y. Bennani, P. Perez-Rodriguez, M.J. Alani, W.A. Smith, L.C. Rietveld, M. Zeman, A.H.M. Smets, Photoelectrocatalytic oxidation of phenol for water treatment using a BiVO4 thin-film photoanode, J. Mater. Res. 31 (2016) 2627–2639, https://doi.org/10.1557/jmr.2016.290.
[72] Y. Lu, Y. Chu, W. Zheng, M. Huo, H. Huo, J. Qu, H. Yu, Y. Zhao, Significant tetracycline hydrochloride degradation and electricity generation in a visible-light-driven dual photoelectrode photocatalytic fuel cell using BiVO4/TiO2 NT photoanode and Cu2O/TiO2 NT photocathode, Electrochim. Acta 320 (2019), 134617, https://doi.org/10.1016/j.electacta.2019.134617.
[73] H. Du, W. Pu, Y. Wang, K. Yan, J. Feng, J. Zhang, C. Yang, J. Gong, Synthesis of BiVO4/WO3 composite film for highly efficient visible light induced photoelectrocatalytic oxidation of norfloxacin, J. Alloys Compd. 787 (2019) 284–294, https://doi.org/10.1016/j.jallcom.2019.01.390.
[74] M.A. Behnajady, B. Vahid, N. Modirshahla, M. Shokri, Evaluation of electrical energy per order (EEO) with kinetic modeling on the removal of malachite green by US/UV/H2O2 process, Desalination 249 (2009) 99–103, https://doi.org/10.1016/j.desal.2008.07.025.
[75] J.R. Bolton, K.G. Bircher, W. Tumas, C.A. Tolman, Figures-of-merit for the technical development and application of advanced oxidation technologies for both electric- and solar-driven systems (IUPAC technical report), Pure Appl. Chem. 73 (2001) 627–637, https://doi.org/10.1351/pac200173040627.